A Method for Introducing Soft Sources in the PSTD Algorithm

Xiang Gao, Mark S. Mirotznik, and Dennis W. Prather

***Abstract*—This paper presents a method for introducing a soft source in the pseudospectral time-domain algorithm. In this method, a scalar weighting term ζ is introduced in the total field/scattered field approach in computational electromagnetics. Using our modified version of Maxwell's equations, soft sources can be introduced simply by adding incident terms in the 8–10-cell connecting region between the total field and the scattered field. One-dimensional (1-D) and two-dimensional (2-D) examples of soft source generation and a 2-D scattering study of a dielectric cylinder are given.**

***Index Terms*—Maxwell's equations, pseudospectral time-domain (PSTD), soft source.**

I. Introduction

RECENTLY, a pseudospectral time domain (PSTD) method was proposed as an efficient algorithm for solving Maxwell's equations [1]–[6]. Unlike the traditional finite-difference-time-domain (FDTD) method, which approximates continuous spatial derivatives using second-order finite differences, the PSTD method uses forward and inverse fast Fourier transforms (FFTs). There are two significant computational advantages in doing so: 1) by using the FFT there is theoretically no spatial dispersion error [1] as found in the traditional FDTD algorithm and 2) only two grid points per minimum wavelength are required in the PSTD method compared to 10–20 typically found in FDTD. Thus, PSTD requires far less memory and is roughly $4^{\mathrm{D}} - 8^{\mathrm{D}}$ (D is the dimensionality) times more efficient than FDTD [1]. Also, the spatial grid is not staggered like the grid used in the FDTD algorithm, so programming is simplified and representation of materials is straightforward. However, there are several issues with the PSTD algorithm with regard to its application in computational electromagnetics [1], [2], [6]. These include: 1) difficulty in dealing with PEC and high contrast materials; 2) difficulty in introducing external soft sources; and 3) modeling of fine structures.

In this paper, we address one of these difficulties, namely the ability to introduce a soft source in the PSTD algorithm. Prior PSTD algorithms [6], [7] have employed a scattered field formulation to deal with continuous soft sources. In a scattered field formulation, the incident terms are needed for the region where the scatters have different material properties to the background. In FDTD, there is a well-developed total field/scattered field (TFSF) formulation, which only requires the incident field components to be calculated along a boundary connecting the TF and SF regions. The TFSF method is easy to implement and does not encumber any significant computational burden. Thus, in this paper we propose a novel approach to introducing continuous soft sources in the PSTD algorithm, while maintaining its computational advantages.

We call our approach the "weighted TFSF" method. To the best of our knowledge, this represents the first application of the TFSF formulation to the PSTD method. To this end, in this paper we first introduce a "connecting region," as oppose to a "connecting boundary" in FDTD between the TF zone and the SF zone. Then we derive the modified Maxwell equations, which pertain to this region. Lastly, numerical examples are given to further show the feasibility of this method.

II. Formulation

For an inhomogeneous conductive medium, we have the following Maxwell curl equations [10]:

$$\begin{cases} \mu \dfrac{\partial \vec{H}}{\partial t} = -\nabla \times \vec{E} - \sigma^* \vec{H} \\ \varepsilon \dfrac{\partial \vec{E}}{\partial t} = \nabla \times \vec{H} - \sigma \vec{E} \end{cases}. \tag{1}$$

Consider the incident wave and scattered wave separately

$$\begin{cases} \vec{E}_{\mathrm{tot}} = \vec{E}_{\mathrm{inc}} + \vec{E}_{\mathrm{scat}} \\ \vec{H}_{\mathrm{tot}} = \vec{H}_{\mathrm{inc}} + \vec{H}_{\mathrm{scat}} \end{cases} \tag{2}$$

where both the incident field and the scattered field satisfy (1).

We now separate the computation region into a total field zone, a scattered field zone, and a connecting region in between. To be mathematically consistent for these three zones we introduce a weight scalar ζ, weighted field components $\hat{\vec{E}}_{\mathrm{tot}}$, $\hat{\vec{H}}_{\mathrm{tot}}$, and weighted incident field components $\hat{\vec{E}}_{\mathrm{inc}}$ and $\hat{\vec{H}}_{\mathrm{inc}}$:

$$\begin{cases} \hat{\vec{E}}_{\mathrm{tot}} = \hat{\vec{E}}_{\mathrm{inc}} + \vec{E}_{\mathrm{scat}} = \zeta \vec{E}_{\mathrm{inc}} + \vec{E}_{\mathrm{scat}} \\ \hat{\vec{H}}_{\mathrm{tot}} = \hat{\vec{H}}_{\mathrm{inc}} + \vec{H}_{\mathrm{scat}} = \zeta \vec{H}_{\mathrm{inc}} + \vec{H}_{\mathrm{scat}} \end{cases} \tag{3}$$

where ζ is chosen to be 0 in the SF zone, 1 in the TF zone, and accordingly continuously change from 0 to 1 in the connecting region. In the SF zone $\hat{\vec{E}}_{\mathrm{tot}} = \vec{E}_{\mathrm{scat}}$, in the TF zone $\hat{\vec{E}}_{\mathrm{tot}} = \vec{E}_{\mathrm{tot}}$, and within the connecting region $\hat{\vec{E}}_{\mathrm{tot}}$ values smoothly connect

Manuscript received March 21, 2003; revised September 10, 2003. This work was supported in part by the Intel Corporation and in part by EM Photonics, Inc.

X. Gao and D. W. Prather are with the Department of Electrical and Computer Engineering, University of Delaware, Newark, DE 19716 USA (e-mail: xigao@ee.udel.edu; dprather@ee.udel.edu).

M. S. Mirotznik is with the Department of Electrical Engineering and Computer Science at The Catholic University of America, Washington, DC 20064 USA (e-mail: Mirotznik@cua.edu).

Digital Object Identifier 10.1109/TAP.2004.831304

the $\vec{E}_{\rm scat}$ field in the SF zone and $\hat{\vec{E}}_{\rm tot}$ field in the TF zone, in order to reduce the Gibbs' phenomenon [8].

After some manipulations of the Maxwell equations and using (3), we obtain the equations for $\hat{\vec{E}}_{\rm tot}$ and $\hat{\vec{H}}_{\rm tot}$

$$\begin{cases} \mu\dfrac{\partial\hat{\vec{H}}_{\rm tot}}{\partial t} = -\nabla\times\hat{\vec{E}}_{\rm tot} - \sigma^*\hat{\vec{H}}_{\rm tot} + \nabla(\zeta)\times\vec{E}_{\rm inc} \\ \varepsilon\dfrac{\partial\hat{\vec{E}}_{\rm tot}}{\partial t} = \nabla\times\hat{\vec{H}}_{\rm tot} - \sigma\hat{\vec{E}}_{\rm tot} - \nabla(\zeta)\times\vec{H}_{\rm inc} \end{cases}. \quad (4)$$

It is interesting to point out that (4) is similar in form to the auxiliary field equations in [11], where a scalar amplitude modulation function $F(r)$ is used to attenuate field values near the computation boundary to achieve reflection-free boundary. In this paper, however, we use ζ to separate the fields and introduce soft sources.

In the TF and SF region where $\nabla\zeta = 0$, (4) is reduced to Maxwell curl equations, and the incident wave information is only required in the connecting region where $\nabla\zeta \neq 0$.

From (4), we can see how the incident wave is introduced into the connecting region, where $\nabla\zeta \neq 0$. (Actually, the name of this method is obtained from the weight scalar ζ). It should be noted that the size of the connecting region must be chosen with care. If the size is excessively small the results may be inaccurate due to Gibbs' phenomenon [8] associated with the abrupt changes in field values and the use of FFT. However, if the connecting region is too large the method will lose much of its computational advantage. So, one must choose a good size for the connecting region to balance efficiency and accuracy. In most cases where error $< 1\times10^{-3}$ is required, a connecting region of a width of 8–10 cells was found to be sufficient. The shape of ζ is also an important factor in reducing Gibbs' phenomenon (and, in turn, reducing errors). Thus, the connecting region serves three purposes: 1) it introduces a soft source; 2) it splits the fields; and 3) it minimizes the Gibbs' phenomenon caused in the transition between the TF zone and the SF zone.

It is also worth noting that the connecting region can be placed in the center of the computation region so that an internal soft source (such as a continuous soft point source, for example) can be introduced.

III. Numerical Results

A. One-Dimensional TM_z Mode Half-Infinite Plane Wave

To illustrate and test our method, 1-D and 2-D examples are given. For the 1-D TM_z mode, we have the following equations obtained from (4):

$$\begin{cases} \mu\dfrac{\partial\hat{\vec{H}}_y}{\partial t} = \dfrac{\partial\hat{\vec{E}}_z}{\partial x} - \sigma^*\hat{\vec{H}}_y - \dfrac{\partial\zeta}{\partial x}\vec{E}_{z\_\rm inc} \\ \varepsilon\dfrac{\partial\hat{\vec{E}}_z}{\partial t} = \dfrac{\partial\hat{\vec{H}}_y}{\partial x} - \sigma^*\hat{\vec{E}}_z - \dfrac{\partial\zeta}{\partial x}\vec{H}_{y\_\rm inc} \end{cases}. \quad (5)$$

To solve (5) numerically using the PSTD algorithm, the spatial derivatives of $\hat{\vec{E}}_z$ and $\hat{\vec{H}}_y$ are obtained from FFT and inverse FFT as [4], [6]

$$\left.\frac{\partial f(x,t)}{x}\right|_{x=x_n} = \frac{1}{N}\sum_{m=0}^{N-1} ik_m\tilde{f}(k_m,t)e^{ik_mx_n} \quad (6)$$

where

$$\tilde{f}(k_m,t) = \sum_{n=0}^{N-1} f(x_n,t)e^{-ik_mx_n}. \quad (7)$$

In (6) and (7), $k_m = 2\pi m/L$, $(m = 0,1,2\ldots N-1)$. But in (6), the first k_m in the right-hand side is forced to be a periodic function within $[-\pi N/L, \pi N/L)$. Unlike the formulas in [4] and [6], by changing the range of the first k_m in (6), there is no need for a grid shift of N/2 for $\tilde{f}(k_m,t)$. This will result in some computational savings. The summations in (6) and (7) are done with the FFT algorithm, which has a computational dependence of $\mathrm{O(N\log_2 N)}$ [9].

The temporal derivatives of weighted field components, $\hat{\vec{E}}_z$ and $\hat{\vec{H}}_y$, are obtained with central difference by staggering the $\hat{\vec{E}}_z$ grid and $\hat{\vec{H}}_y$ grid in time domain, the same as in the FDTD method [1].

A half-infinite plane wave with a smooth front is used as the incident wave. We use a raised cosine function to smooth the front of the incident wave. For an infinite plane wave, we have

$$\begin{aligned} H_{y\_\rm inc}(t) &= -\sqrt{\frac{\varepsilon_0}{\mu_0}}\cos[\omega t - k\cdot x] \\ E_{z\_\rm inc}(t) &= \cos\left[\omega\left(t\pm\frac{dt}{2}\right) - k\cdot x\right]. \end{aligned} \quad (8)$$

Equation (8) is then multiplied with a proper envelope function to become a traveling half-infinite plane wave. The term $dt/2$ in (8) is due to the fact that the temporal grids of $\vec{E}_{z\_\rm inc}$ and $\vec{H}_{y\_\rm inc}$ are staggered with a $dt/2$ interval. The sign of the $dt/2$ term is determined by the updating sequence of $\hat{\vec{E}}_z$ and $\hat{\vec{H}}_y$ in the computation program. The wavenumber k in (8) is given by the dispersion relationship [1]

$$k = \frac{2}{c\Delta t}\sin\frac{\omega\Delta t}{2} \quad (9)$$

to effectively minimize numerical dispersions due to the temporal finite difference approximation (recall that the spatial discretization does not introduce any numerical dispersion in the PSTD algorithm).

The weight function ζ is constructed from a smooth function $y(x)$, its mirror image $y(-x)$ and functions of constant 1 and 0. See illustration in Fig. 1(a). Smooth function $y(x)$ has a value of 0 on one end and a value of 1 on the other. Our choices for $y(x)$ include a raised cosine function, half of a Gaussian distribution curve, half of a Blackman–Harris (BH) window function, and an integral form of the BH (IBH) window function. Fig. 1(a) shows such smooth functions $y(x)$ and ζ. Fig. 1(b) shows the Fourier spectrums of weight function ζ constructed from different $y(x)$. The best choice for $y(x)$ (and ζ) is the one that has the smallest high spatial frequency components that extends beyond the highest frequency value, which is $\pm1/(2\Delta x)$ in FFT. And indeed, we have found that IBH window function, which offers $< 1\times10^{-4}$ errors with eight cells, is the best choice. This window function will be discussed in detail in Section IV.

Because in (3), ζ is multiplied to the incident terms, its shape will affect the derivative calculations of $\hat{\vec{E}}_{\rm tot}$ and $\hat{\vec{H}}_{\rm tot}$ in (4) using the FFT/iFFT method. To study this effect, we multiply

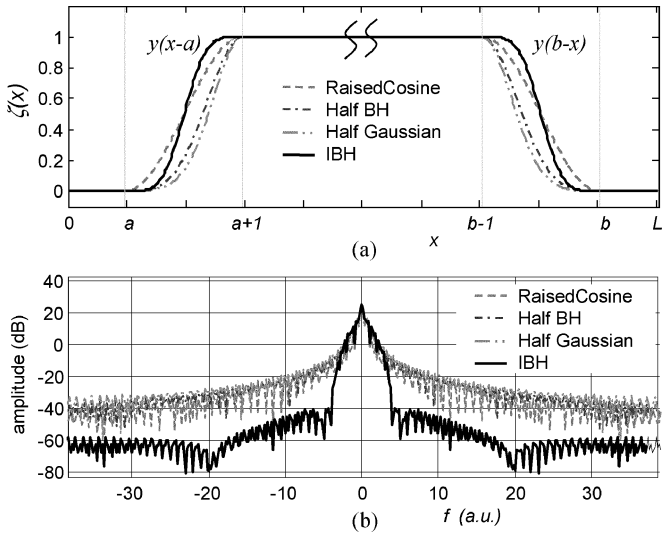

Fig. 1. (a) Diagram of several functions used to construct ζ. (b) The Fourier spectrum of the corresponding weight function ζ. The integral form of the Blackman–Harris (IBH) function offers the smallest side lobes.

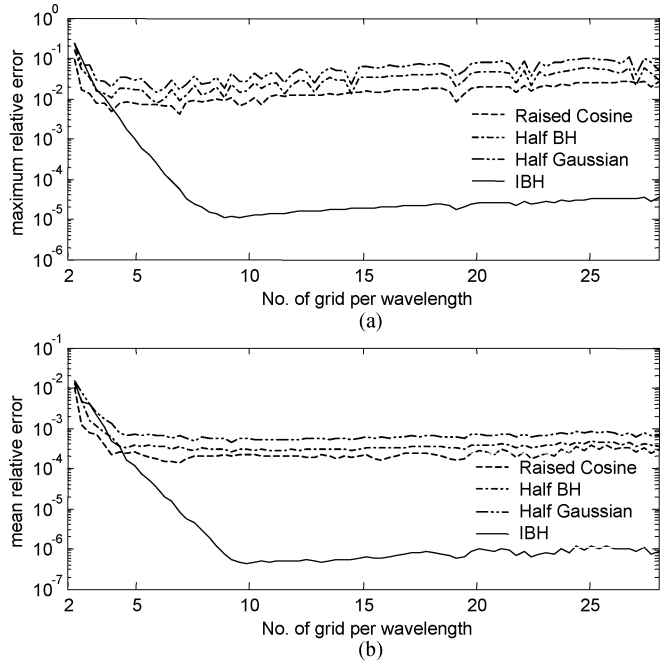

Fig. 2. Relative errors in derivative calculations using FFT/IFFT on a sinusoidal function multiplied by ζ. The connecting region has a grid thickness of 10 cells. (a) The maximum relative error versus the sampling rate. (b) The mean relative error versus the sampling rate.

a single-wavelength sinusoidal function by ζ as a test function, and obtain the relative errors in derivative calculations with the FFT/iFFT method. The results are shown in Fig. 2. For very small sampling rate, it shows large errors and as sampling rate increases the errors reduce and stabilize for higher frequency ranges. The maximum relative error values plotted in Fig. 2(a) are the overshoots in the Gibbs' phenomena. Clearly IBH window function offers the best performance. In all following simulations, we use IBH for the weight function ζ.

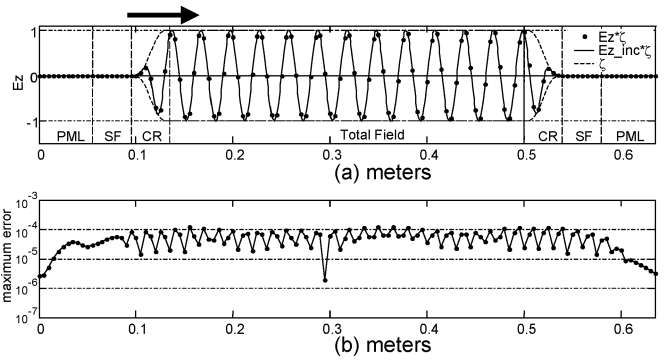

Fig. 3. (a) E_z component and ζ for a 10 GHz plane wave traveling in free space along the $x+$ direction. Dots are calculated with the "weighted TFSF" PSTD algorithm. Solid line is the known incident wave, whose value is added only in the CR (connecting region). (b) The maximum error recorded during a long enough time period. The error is the difference between the numerical values and known incident values.

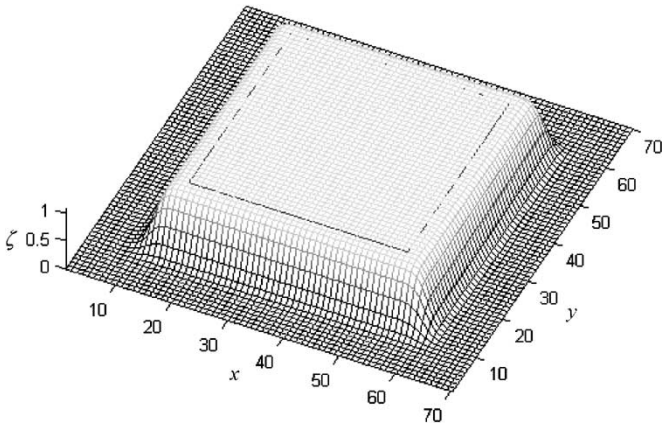

Fig. 4. Diagram of ζ for the 2-D case, with $\zeta = \zeta_x \zeta_y$. A large connecting region is intentionally used for illustration purposes.

There are two ways to obtain the derivatives of ζ: One can use the analytical values, since ζ is given analytically; or one can use the FFT/iFFT technique to numerically obtain the derivatives. In our simulations, we used the second technique. To keep the computational advantage, only the derivative values inside the connecting region are used, the rests are omitted. We found that the second technique can help reduce the Gibbs' phenomenon.

In our numerical experiment with 1-D soft source generation, we created a plane wave in vacuum with $f = 10$ GHz, using 128 grid points with a grid density of six grids per λ_0. (λ_0 is the free space wavelength). An eight-cell connecting region and a 12-cell PML are used, and their borders are indicated in Fig. 3(a). The time step is set as $\Delta t = \lambda_0/20c$, which in our case satisfies the stability condition: $\Delta t < \Delta x/1.57c$ (1-D case in [1] and [4]). Fig. 3(a) shows the weight function ζ and normalized E_z component of the 1-D TM_z mode. The maximum numerical errors recorded during a long enough time period are plotted in Fig. 3(b), and are shown to be less than 1×10^{-4}.

B. Two-Dimensional TE_z *Mode Half-Infinite Plane Wave*

In the 2-D case, we used the split field PML equations for 2-D TE_z plane wave incidence. After using the transform, $H_{\mathrm{new}} =$

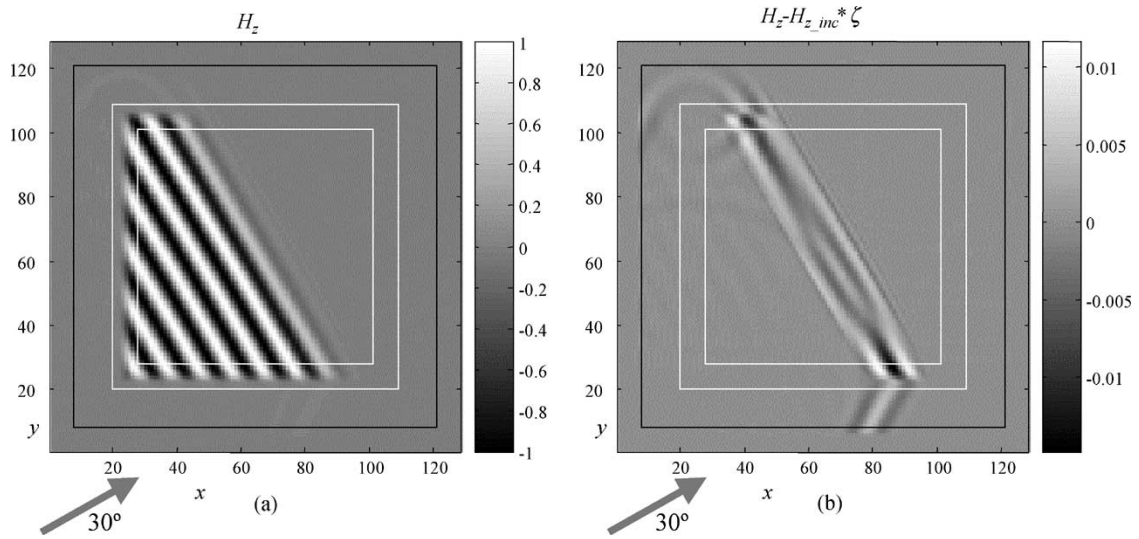

Fig. 5. (a) Snap shot of H_z of a half-infinite plane wave at 30° incident angle, shortly after the wave front appeared in the computing region. (b) The error of H_z, at the same time. As can be seen the wave front is associated with a large error, mainly due to the fact that dispersion at the wave front is different to dispersion at the steady state.

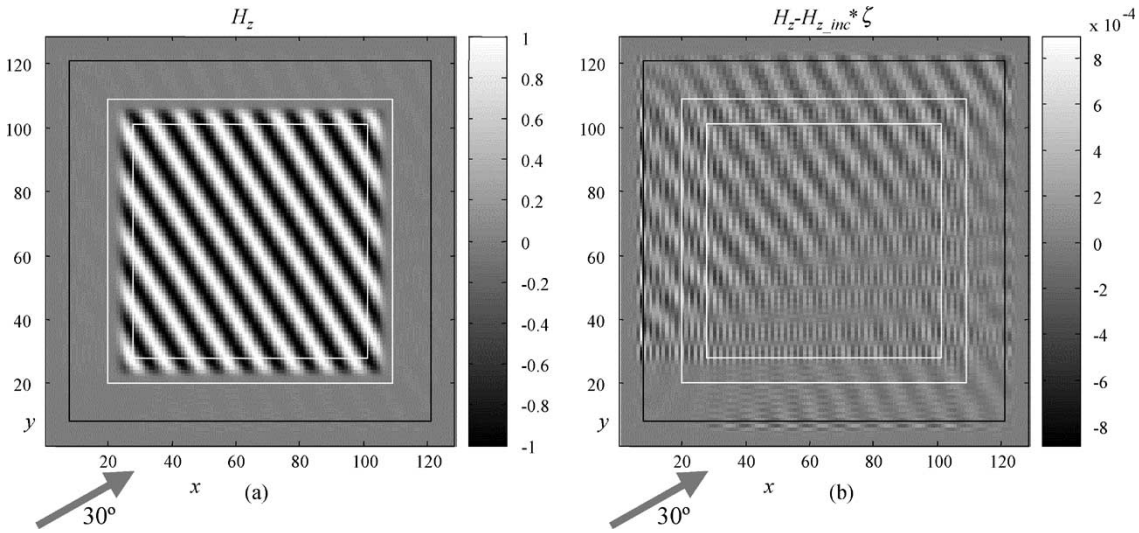

Fig. 6. (a) Snap shot of H_z of a half-infinite plane wave at 30° incident angle, after $t > 2 * L_x/c$. (L_x/c is the time for light to propagate across the x dimension). (b) The error of H_z, at the same time.

$Z_0 H_{\text{old}} = \sqrt{\mu_0/\varepsilon_0} H_{\text{old}}$ and some derivations from the ordinary split field PML equations [10], we obtain the following equations for the weighted $\widehat{\widehat{E}}$ and $\widehat{\widehat{H}}$ fields:

$$\begin{cases} \dfrac{\partial \widehat{E}_x}{\partial t} = \dfrac{c}{\varepsilon_r}\left(\dfrac{\partial \widehat{H}_z}{\partial y} - \dfrac{\partial \zeta}{\partial y} H_{z\_\text{inc}}\right) - \dfrac{\sigma_y}{\varepsilon_r \varepsilon_0}\widehat{E}_x \\ \dfrac{\partial \widehat{E}_y}{\partial t} = -\dfrac{c}{\varepsilon_r}\left(\dfrac{\partial \widehat{H}_z}{\partial x} - \dfrac{\partial \zeta}{\partial x} H_{z\_\text{inc}}\right) - \dfrac{\sigma_x}{\varepsilon_r \varepsilon_0}\widehat{E}_y \\ \dfrac{\partial \widehat{H}_{zx}}{\partial t} = -\dfrac{c}{\mu_r}\left(\dfrac{\partial \widehat{E}_y}{\partial x} - \dfrac{\partial \zeta}{\partial x} E_{y\_\text{inc}}\right) - \dfrac{\sigma_x^*}{\mu_r \mu_0}\widehat{H}_{zx} \\ \dfrac{\partial \widehat{H}_{zy}}{\partial t} = \dfrac{c}{\mu_r}\left(\dfrac{\partial \widehat{E}_x}{\partial y} - \dfrac{\partial \zeta}{\partial y} E_{x\_\text{inc}}\right) - \dfrac{\sigma_y^*}{\mu_r \mu_0}\widehat{H}_{zy} \end{cases} \tag{10}$$

where $\widehat{H}_z = \widehat{H}_{zx} + \widehat{H}_{zy}$ and $\widehat{S} = \zeta S_{\text{inc}} + S_{\text{scat}}$. In this case, S represents the E and H components.

Fig. 4 is a 3-D diagram of ζ. For illustration purpose, a very thick connecting region is used. Because of the rectangular geometry of the connecting region, we simply use $\zeta = \zeta_x \cdot \zeta_y$ to construct ζ. Both ζ_x and ζ_y are formed from the IBH window function [see Fig. 1(a)].

Figs. 5 and 6 show snap shots for an angled half-infinite TE_z mode plane wave with unit amplitude traveling in vacuum. The computation region has $N_x \times N_y = 128 \times 128$ grid points. An eight-cell PML and an eight-cell connecting region are used, and their borders are indicated as concentric boxes shown in Fig. 5 and 6. To display the wave, roughly nine grid points per λ_0 are used. The time step is set as $\Delta t = \lambda_0/20c$, which in our case satisfies the stability condition: $\Delta t < \Delta x/2.221c$ (2-D case in [1] and [4]). The numerical errors, which are defined as the difference between the PSTD numerical value and the known incident value, are shown in Figs. 5(b) and 6(b). Due to the fact that numerical dispersion is only compensated at λ_0 and the wave front contains other spatial frequency components, the numerical dispersion artifact is not completely eliminated, as

can be seen in Fig. 5(b). However after the wave front passed the computation region, it has much smaller errors, as shown in Fig. 6(b). We believe the remaining numerical errors result mostly from the Gibbs' phenomenon associated with the PML and the connecting region.

C. Scattering of a Dielectric Cylinder With 2-D TM_z Mode Plane Wave Incidence

We also studied the scattering of an incident plane wave from a dielectric cylinder. The cylinder is assumed to be isotropic, homogeneous with a relative electric permittivity $\varepsilon_r = 2.25$, a relative magnetic permeability $\mu_r = 1$, and a radius of 8 m. A half-infinite TM_z mode plane wave soft source is generated with the same technique explained in Section III-B, with an eight-cell PML and an eight-cell connecting region. The incident wave has a free space wavelength λ_0 of 1 m, and a 0° incident angle along the x axis. Size of the computation region is $L_x \times L_y = 30 \times 30$ m. To represent the circular cylinder boundary with good fidelity in an orthogonal grid, we use a grid of $N_x \times N_y = 512 \times 512$. This corresponds to roughly 11.38 grids per wavelength in the cylinder. A time step of $\lambda_0/40c \cong 8.33 \times 10^{-11}$ (s) is used.

Steady state is achieved when the incident wave has traveled a length of more than five times the diameter of the cylinder. The steady state value of the weighted $\hat{E}_z$ component is given in Fig. 7. The rectangular boxes in Fig. 7 indicate the borders of the PML and connecting region. The PSTD value $\hat{E}_{z\_\mathrm{PSTD}}$ is then compared with analytical solutions E_{z_analytic}. The absolute error, which is defined as $|\hat{E}_{z\_\mathrm{PSTD}} - \zeta E_{z\_\mathrm{analytic}}|$, is shown in Fig. 8. As can be seen, large errors are mostly located near the surface of the cylinder. This is primarily due to Gibbs' phenomenon at the interface where the derivatives of the tangential field values along the longitudinal direction are not continuous. This is one of the limiting factors when applying the PSTD method to materials with large dielectric contrast. The problem of representing a circular boundary with an orthogonal grid also affects the accuracy near the boundary. But interestingly there is little error outside the cylinder. Fig. 9 shows a line scan of the field values at a radius of 12 m to the center of the cylinder. As can be seen in Fig. 9, the weighted TFSF PSTD method gives almost identical results as the analytical method.

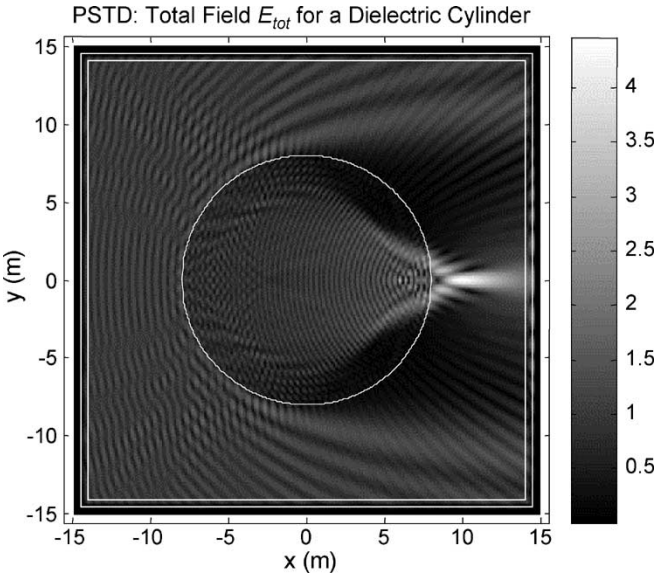

Fig. 7. Scattering of a dielectric cylinder with refractive index of 1.5 and radius of 8 m. Other parameters are given in the text in Section III-C.

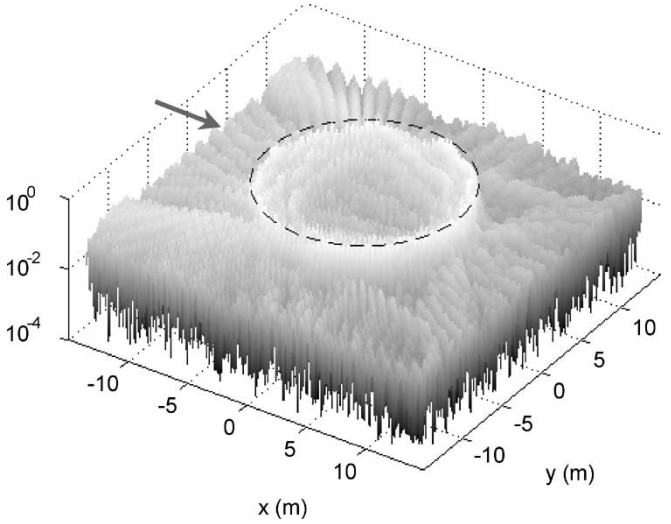

Fig. 8. Absolute error of E_z. The dotted circle shows the surface of the dielectric cylinder. The arrow indicates the propagation direction of the incident wave. Simulation parameters are given in the text in Section III-C.

IV. Discussion

In popular 2-D or 3-D FDTD TFSF methods, the 1-D propagation equation is solved first by using FDTD with the same grid size and time step. Then, the values of the incident plane wave are interpolated from the 1-D solution. The FDTD typically uses more than 16 grid points per wavelength so the interpolation can be done quite accurately. But for the PSTD, which usually uses fewer grid points per wavelength, the use of the same interpolation technique may not be a good solution. Fortunately, the numerical dispersion relation for PSTD is isotropic [1]. In fact, our numerical experiments confirm that by using the numerical dispersion relationship derived in [1], dispersion errors can be effectively eliminated for a steady state computation. But for the front of the incident wave, because different frequency components exist, the dispersion formula cannot work effectively, see Fig. 5(b). We believe that using interpolation from the spectral components of a 1-D propagation might solve this problem.

In our numerical experiments on plane wave propagation, the Gibbs' phenomenon introduced by ζ is the main source of numerical errors. To find the optimum curve with minimal Gibbs' phenomenon, we have tried several window functions to construct ζ. We have found that the integral form of the BH window function renders the best performance. The BH window function, which is well known in the digital signal processing community, can be written as

$$BH(x) = \sum_{k=0}^{M} a_k \cos(2\pi k x) \tag{11}$$

where x is within the range [0 1] and $M + 1$ is the number of terms for the BH window function. Usually the BH window function is bell shaped. For a 92 dB suppression of the first side

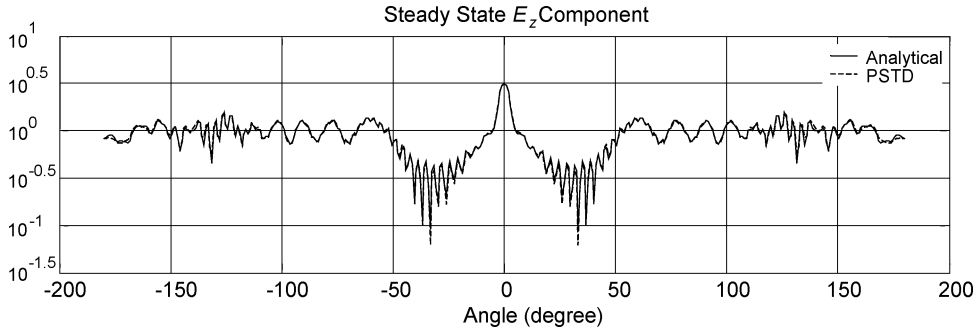

Fig. 9. Comparison of analytical values and PSTD values for the steady state E_z component at a radius of 12 m.

lobe, we have $a_0 = 0.358\,75$, $a_1 = -0.488\,29$, $a_2 = 0.141\,28$, $a_3 = -0.011\,68$.

The integral form of the BH function is

$$\mathrm{IBH}(x) = \sum_{k=0}^{M} a_k \frac{\sin(2\pi k x)}{2\pi k}. \tag{12}$$

This function changes smoothly from 0 to a_0, as x changes from 0 to 1. In our numerical experiments, we use $a_0 = 1$, $a_1 = -1.3611$, $a_2 = 0.3938$, $a_3 = -0.0326$, which is obtained by simply normalizing a_k to a_0. A simple analysis in the spectral domain reveals that, for $M+1$ nonzero terms in the IBH window function, a minimum of $2(M+1)$ grid points are required to effectively contain the main lobe of the spectrum of ζ. In the 1-D case, with ζ constructed from our choice of a_k and (12), the numerical errors due to Gibbs' phenomenon can be effectively reduced to less than 1×10^{-4} with only eight cells for the connecting region (see Fig. 3).

In our studies on the scattering in the presence of a dielectric cylinder with the PSTD method, we found that because the material properties change abruptly, a grid density much larger than the Nyquist sampling rate is needed to ensure accuracy. From this we conclude that more research is needed to obtain accurate simulation results with a coarse grid for problems involving materials with high contrast and objects with fine structures.

An important observation we made from our numerical experiments is that the weight function produces errors due to the Gibbs' phenomenon introduced by itself (see Figs. 1 and 2). We can make a similar conclusion for the PML as well. Because PML attenuates the wave functions, it broadens the spectral contents of the wave functions inside the computation region. In order to contain the Gibbs' phenomenon created by the PML, one has to use a sampling rate higher than the Nyquist sampling rate. Additional research is needed to find the optimum grading in PML structures to reduce the spectral broadening effect.

It should be noted that, although our method is proposed for the application of Fourier PSTD algorithm, the weighted TFSF method is algorithm independent, which is apparent from the derivations of (4).

V. Conclusion

We have developed a new method to introduce continuous soft-sources into the PSTD algorithm for analyzing the wave scattering in an inhomogeneous medium. We provided 1-D and 2-D PML examples to support our findings. These numerical experiments have confirmed the validity of such a method. Moreover, since the additional terms found in our modified Maxwell's equations required computing the incident fields only in the connecting region, our method was found to be easy to implement and efficient.

Acknowledgment

The authors would like to thank Prof. S. ShouYuan in the Department of Electrical and Computer Engineering, University of Delaware, Newark, for helpful discussions in PSTD and FDTD methods.

References

[1] Q. H. Liu, "The PSTD algorithm: a time-domain method requiring only two cells per wavelength," *Microw. Opt. Technol. Lett.*, vol. 15, no. 3, pp. 158–165, June 1997.

[2] ——, "PML and PSTD algorithm for arbitrary lossy anisotropic media," *IEEE Microwave Guided Wave Lett.*, vol. 9, no. 2, Feb. 1999.

[3] ——, "A frequency-dependent PSTD algorithm for general dispersive media," *IEEE Microwave Guided Wave Lett.*, vol. 9, Feb. 1999.

[4] ——, "Large-scale simulations of electromagnetic and acoustic measurements using the pseudospectral time-domain (PSTD) algorithm," *IEEE Trans. Geosci. Remote Sensing*, vol. 37, pp. 917–926, Mar. 1999.

[5] Y. F. Leung and C. H. Chan, "Pseudospectral time-domain (PSTD) method with unsplit-field PML," *Microw. Opt. Technol. Lett.*, vol. 22, no. 4, pp. 278–283, Aug. 1999.

[6] Q. L. Li, Y. C. Chen, and D. Ge, "Comparison study of the PSTD and FDTD methods for scattering analysis," *Microw. Opt. Technol. Lett.*, vol. 25, no. 3, pp. 220–226, May 2000.

[7] G. X. Fan and Q. H. Liu, "Pseudospectral time-domain algorithm applied to electromagnetic scattering from electrically large objects," *Microw. Opt. Technol. Lett.*, vol. 29, no. 2, pp. 123–125, Apr. 2001.

[8] D. Gottlieb and S. A. Orszag, *Numerical Analysis of Spectral Methods: Theory and Applications*. Philadelphia, PA: SIAM, 1977.

[9] R. N. Bracewell, *The Fourier Transform and Its Applications*, 2nd ed. New York: McGraw-Hill, 1986.

[10] A. Taflove and S. C. Hagness, *Computational Electrodynamics: The Finite-Difference Time-Domain Method*, 2nd ed. Norwood, MA: Artech House.

[11] J. Peng and C. A. Balanis, "A generalized reflection-free domain-truncation method: Transparent absorbing boundary," *IEEE Trans. Antennas Propagat.*, vol. 46, pp. 1015–1022, July 1998.

Xiang Gao received the M.S. degree in semiconductor physics from Nanjing University, Nanjing, China, in 1997 and the M.S. degree in electrical engineering from the University of Delaware, Newark, in January 2000, where he is currently working toward the Ph.D. degree in the Department of Electrical and Computer Engineering.

Between February 2000 and June 2002, he worked in the photonic and telecommunication industry as a Research Engineer.

Mark S. Mirotznik received M.S. degrees in biomedical and electrical engineering and the Ph.D. degree in biomedical engineering from The University of Pennsylvania, Philadelphia, in 1991 and 1992, respectively.

He is currently an Associate Professor of electrical engineering at The Catholic University of America, Washington, DC. His research is in the areas of computational electromagnetics and microphotonics with biomedical applications.

Dennis W. Prather is an Associate Professor in the Department of Electrical and Computer Engineering, University of Delaware, Newark. There, he has established the Laboratory for Nano- and Integrated-Photonic Systems. In this lab, they focus on both the theoretical and experimental aspects of active and passive nanophotonic elements and their integration into optoelectronic subsystems. To achieve this, his lab develops and refines computational electromagnetic tools for both the analysis and synthesis of photonic devices. In addition, they also develop nanofabrication and integration processes necessary for their integration into functional subsystems. Devices of particular interest include subwavelength structures, photonic crystal devices, diffractive optical elements, and optical waveguides for application in next generation optoelectronic systems.